EXPERIMENTALLY VERIFIED MODEL OF ELECTROSTATIC ENERGY HARVESTER WITH INTERNAL IMPACTS

Binh Duc Truong, Cuong Phu Le, and Einar Halvorsen
University College of Southeast Norway

IEEE International Conference on Micro Electro Mechanical Systems. 2015, (February), 1125-1128.

EXPERIMENTALLY VERIFIED MODEL OF ELECTROSTATIC ENERGY HARVESTER WITH INTERNAL IMPACTS

Binh Duc Truong, Cuong Phu Le, and Einar Halvorsen
Department of Micro- and Nano Systems Technology, Buskerud and Vestfold University College, Campus Vestfold, Raveien 215, 3184 Borre, NORWAY

ABSTRACT

This paper presents experimentally verified progress on modeling of MEMS electrostatic energy harvesters with internal impacts on transducing end-stops. The two-mechanical-degrees-of-freedom device dynamics are described by a set of ordinary differential equations which can be represented by an equivalent circuit and solved numerically in the time domain using a circuit simulator. The model accounts for the electromechanical nonlinearities, nonlinear damping upon impact at strong accelerations and the nonlinear squeezed-film damping force of the in-plane gap-closing transducer functioning as end-stop. The comparison between simulation and experimental results shows that these effects are crucial and gives good agreement for phenomenological damping parameters. This is a significant step towards accurate modeling of this complex system and is an important prerequisite to improve performance under displacement-limited operation.

INTRODUCTION

Vibration energy harvesting to power wireless sensor systems and microelectronic applications can eliminate use of batteries which have negative impacts on device size, achievable operational lifetimes and the environment. By scavenging surrounding vibration energy and converting into electrical energy, the system is enabled to operate autonomously [1-2]. Commonly, a harvester's architecture is a spring-mass systems with a transducer based on either three mechanisms: piezoelectric, electrostatic and electromagnetic conversion. Proof mass motion under ambient vibrations induces electromechanical transduction that generates power. For such resonant device structures with high mechanical quality factor Q, use of rigid end-stops to confine maximum amplitude of the proof mass displacement under strong vibration is applicable. Many works have exploited impact on the end-stops to enhance system bandwidth. However, an undesirable consequence remains power saturation when the displacement limit is reached [3-6].

In our previous works, we have experimentally demonstrated a device concept that utilizes sub-transducers functioning as soft end-stops to collect extra power adding to that of the main transducers [7-8]. The technique can be considered as an alternative to the load optimization used for the canonical generators [9]. The measurement result shows that achieved power continues to increase even when large vibration drives the proof mass displacement to the limit. Hence, this approach overcomes a major limitation of conventional harvester designs that experience saturated power with use of rigid end-stops. The prototype performance exhibits strong nonlinearities because of the collisions between the main proof mass and the end-stop transducer in the impact regime. These severe and complex nonlinearities make the impact device hard to model. A simple lumped-model was studied to predict the nonlinearities for this type of device in [10]. Although the model is able to capture the main aspects of device behavior, there are still significant differences between the measured and simulated results, which can be attributed to inadequately modelled damping.

In this work, we investigate effects of the nonlinear damping caused by the impact force and the squeeze-film air damping in the gap-closing capacitance structures of the end-stop transducer.

ANALYSIS AND MODELING

Impact-based device concept

The device concept with transducing end-stop is shown in Figure 1a. The motion of the main proof mass is limited by maximum amplitude of X_{max}, while its relative distance to the transducing end-stop at equilibrium position is x_1. The maximum possible displacement amplitude of the end-stop transducer is $x_2=X_{max}-x_1$. When the main proof mass reaches x_1, the end-stop transducer is activated and generates additional electrical power beyond that generated by the main transducers.

Figure 1b shows key features of the impact device design using electrostatic conversion for all transducers. The main transducer consists of two anti-phase transducers with overlap-varying capacitances. The end-stop transducer is desired to effectively harvest energy from the impact. Thus, the end-stop transducer uses gap-closing capacitance to have high coupling. Two moving structures are suspended by linear folded-springs and have the same direction of in-plane movement. Figure 1c displays a close-up view of the fabricated device using SOIMUMPs process with a layer thickness of t=25 μm and an active area of 4x5 mm^2. All design parameters of the prototype can be found in [7].

Lumped-model

All transducers operate in the continuous mode, separately biased by a voltage source V_p for the main transducers and a voltage source V_s for the end-stop transducer. All fixed electrodes are connected to the external loads.

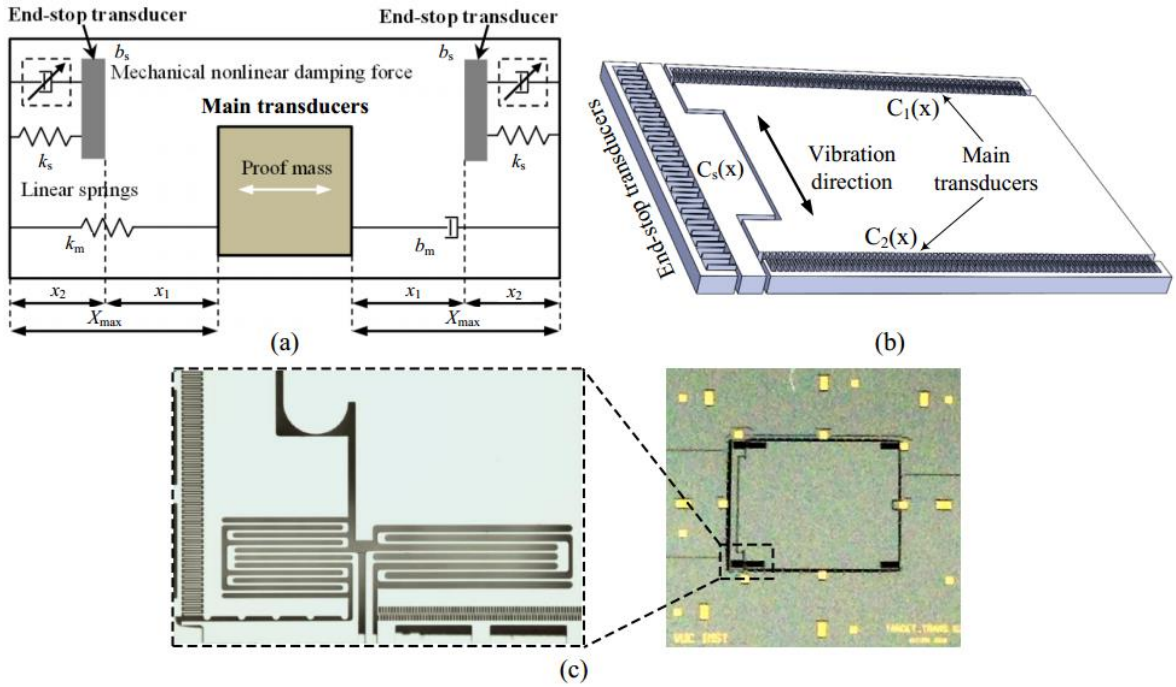

Figure 1: (a) A drawing illustration of device concept with use of end-stop transducer as an additional harvester, (b) key features of the electrostatic device and (c) a close-up view of the MEMS prototype fabricated in the SOIMUMPs process

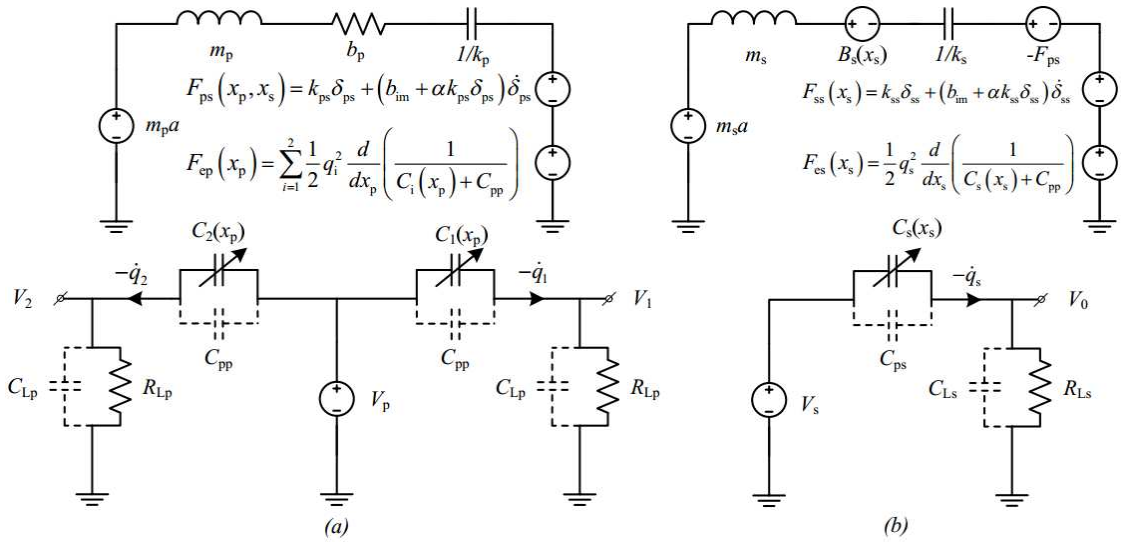

Figure 2: Equivalent-circuit model of the impact device: (a) main transducers and (b) end-stop transducer

The lumped-model of the impact device has the equivalent circuits shown in Figure 2. The model has two degrees of freedom: displacement x_p of the main proof mass and displacement x_s of the end-stop mass. The mechanical and electrical domains are captured by

$$m_p\ddot{x}_p + b_p\dot{x}_p + k_p x_p + F_{ps}(x_p, x_s) + F_{ep}(x_p) = m_p a \quad (1)$$

$$V_p = -\frac{q_{1/2}}{C_{1/2}(x_p) + C_{pp}} + V_{1/2} \quad (2)$$

for the main transducers and by

$$m_s\ddot{x}_s + B_s(x_s) + k_s x_s - F_{ps}(x_p, x_s) + F_{ss}(x_s) + F_{es}(x_s) = m_s a \quad (3)$$

$$V_s = -\frac{q_s}{C_{1/2}(x_p) + C_{ps}} + V_0 \quad (4)$$

for the end-stop transducer. $q_{1/2}$ and q_s are the charges on the main transducers and the end-stop transducer respectively. The transducer electrostatic forces are $F_{ep}(x_p)$ and $F_{es}(x_s)$ while the mutual force that arises from the internal impacts is denoted $F_{ps}(x_p, x_s)$. $F_{ss}(x_s)$ is the impact force between the movable and the rigid end-stops at the ultimate displacement. δ_{ps} and δ_{ss} are the deformation displacements between the main proof mass and the end-stop proof mass, and between the end-stop proof mass and the rigid end-stops during impact respectively. Stray capacitances are also included in the model. The mechanical damping force in the end-stop transducer is $B_s(x_s)$ while that of the main transducers is dominated by slide film damping $b_p\dot{x}_p$.

All nonlinear forces are implemented as behavioral sources in the circuit simulator. There are three types of sources of nonlinearities considered in the lumped-model: i) the electrostatic forces $F_{ep}(x_p)$ and $F_{es}(x_s)$, ii) the damping force $B_s(x_s)$ due to squeeze-film damping in the

gap-closing end-stop transducer and iii) the impact forces $F_{ps}(x_p, x_s)$, $F_{ss}(x_s)$.

Squeeze-film damping force

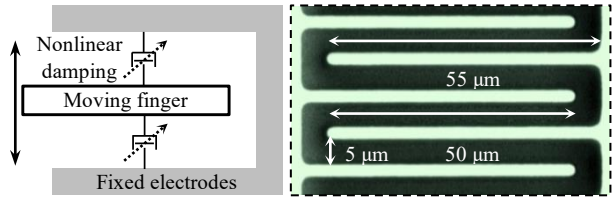

Figure 3: Squeeze film air damping between moving and fixed electrodes in end-stop transducer

Figure 3 shows the electrode structure of the end-stop transducer. In the layout, the nominal gap between fingers is g_0=5.0 μm and the minimum gap is 1.0 μm. When the impact force drives the gap size sufficiently small, the squeeze-film damping force is a major factor opposing motion of the end-stop transducer. In modelling, we consider the thin air film incompressible. The damping force follows the linearized Reynolds equation in the operational frequency range. Including the squeeze-film damping of the gap-closing capacitor structure [11] and an additional phenomenological linear damping, the total damping force of the end-stop transducer is

$$B_s(x_s) = b_g(x_s)\dot{x}_s \tag{5}$$

where

$$b_g(x_s) = b_l + \frac{b_n}{\left(1-\frac{x_s}{g_0}\right)^3} + \frac{b_n}{\left(1+\frac{x_s}{g_0}\right)^3} \tag{6}$$

$$b_n = 2N_g\mu\frac{Lt^3}{g_0^3} \tag{7}$$

N_g is the number of fingers, L is the nominal finger overlap and b_l is the linear damping coefficient.

Impact forces

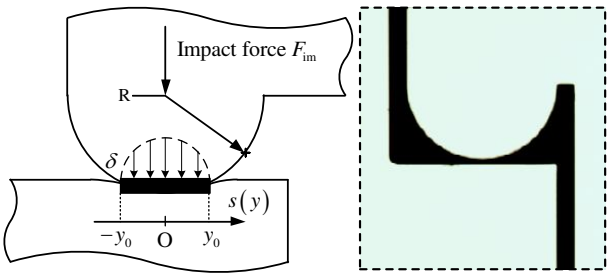

Figure 4: Impact region between the main proof mass and the end-stop proof mass

Figure 4 shows the impact region between the two masses. The impact shape is a line contact between semi-cylindrical bumps and flat surfaces. Thus, the impact force can be found based on Hertz's contact problem and nonlinear viscoelastic model that simultaneously accounts for the coefficient of restitution and the initial impact velocity. However, the latter component is very hard to define due to extremely complex interplay between two moving structures. We assume operation of the impact device in regimes of low frequency and small impact velocity. Hence, the nonlinear impact force can be simplified as [12]

$$F_{im} = k_{im}\delta + \left(b_{im} + \alpha k_{im}\delta\right)\dot{\delta} \tag{8}$$

where k_{im} is the impact stiffness, b_{im} and α are damping coefficients accounting for the impact losses.

While the damping coefficients of the impact force are found by fitting to measurement, the impact stiffness is estimated by static analysis of the Hertz's contact, giving by the following equation [13]

$$\delta = \frac{2\lambda F_{im}}{t}\left[1 + \ln\frac{t^3}{2\lambda F_{im}R}\right] \tag{9}$$

where $\lambda = \frac{1-\upsilon^2}{\pi E}$, E is the Young's modulus, υ is the Poison's ratio and R the radius of cylinder. For a small range of the deformation, Eq. (9) can be linearized by an approximated stiffness $k_{im} \approx 0.058\frac{\pi E t}{1-\upsilon^2}$ [14]. For comparison, the linear damping written in a spring-damper model of the impact force $F_{im} = k_{im}\delta + b_{im}\dot{\delta}$ is studied in simulation.

RESULTS AND DISCUSSION

The model parameters are found based on the design layout and fitting to the measurement results in both the linear regime and the impact regime. All parameters of the prototype model are given in Table 1.

Table 1: Model parameters of the impact device

Parameters	Main transducer	End-stop transducer
Proof mass	m_p=1.15 mg	m_s=0.05 mg
Spring stiffness	k_p=18.2 N/m	k_p=16.3 N/m
Thin-film air damping	b_p=1.50e-5 Ns/m	b_l=1.10e-5 Ns/m b_n=6.18e-5 Ns/m
Impact damping	b_{im}=5.38 Ns/m, α = 4.5	
Nominal capacitance	C_{0p}=1.08 pF	C_{0s} =1.30 pF
Parasitic capacitance	C_{pp}=7.50 pF	C_{ps}=4.00 pF
Load resistance	R_{Lp}=18.5 MΩ	R_{Ls}=18.5 MΩ
Load capacitance	C_{Lp}=4.20 pF	C_{Ls}=4.20 pF
Impact stiffness	k_{ps}=3.26e6 N/m, k_{pp}=8.08e6 N/m	

Figure 5 compares measurement and simulation results for various excitation levels. For A=0.021 g and 0.057 g, the main proof mass displacement is far below the limit, giving no impact. The linear response of the impact device provides a subset of the model parameters, while the remaining parameters of the nonlinear damping force and the impact force are obtained from fitting to experiment results in the impact regime. Higher accelerations A=0.318 g and A=0.707 g leads to increased impact intensities. The strong impacts make the displacement waveforms irregular. This irregularity is manifest also in the average power in the figure. The simulation shows that the dynamics are still well-captured by the model with the nonlinear damping impact force, but there is a slight deviation observed for the model of the linear damping impact force. The difference indicates that the nonlinear model of the impact force has made

improvement over the linear one in reproducing the complex behavior of the impact device.

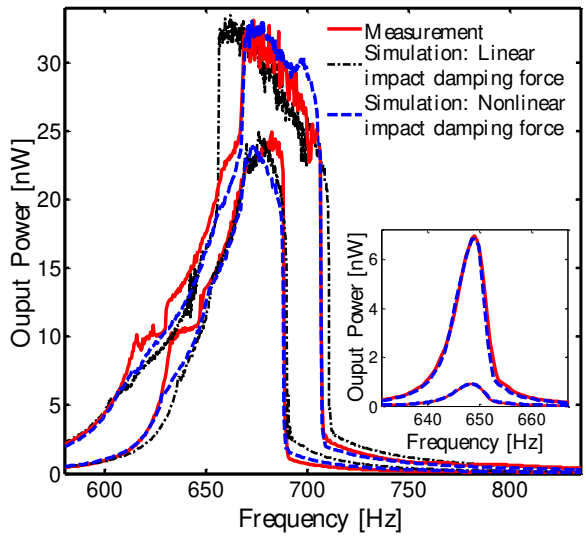

Figure 5: Total power in impact regime for A=0.318 g *and* 0.707 g *at bias voltage of* V_p=V_s=9.2 V. *Subfigure shows frequency responses in linear regime for* A=0.021 g *and* 0.057 g

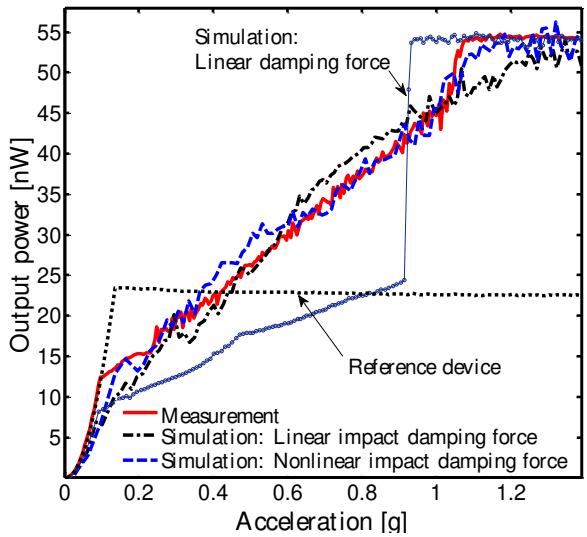

Figure 6: Total power of the impact and reference devices at their resonant frequencies under acceleration sweep for V_p=9.2 V *and* V_s=14.5 V

The obtained power of the impact device is enhanced in the impact regime when the transducer end-stop is more compliant. This can be done by electric control of the bias voltage V_s as demonstrated in our previous work [9]. Figure 6 shows validation of the model under the acceleration sweep when the effective stiffness of the end-stop transducer is significantly reduced when V_s=14.5 V. Both experiment and simulation results show power about 2.4 times higher than that of a standard reference device of the same size and with identical operating conditions. At small excitation (linear regime), the main proof mass displacement is too small to engage end-stops, giving total power mostly from the main transducers. Sufficient acceleration amplitude leads to the impact and extra power from the end-stop transducer contributing to the total power which grows like linearly before the maximum value is reached. The simulation agrees with the measurement when the effects of the impact nonlinearity and the nonlinear squeeze-film damping force are included, while a considerably different response exhibiting a clear jump phenomenon results from use of a mere linear damping-force model for the end-stop transducer.

CONCLUSION

The impact device with the end-stop transducer has proven advantages over conventional designs with rigid end-stops. The improved power is achieved from the internal impact mechanism to overcome the well-known phenomenon of power saturation. The prototype performance was verified by a lumped-model built that is able to capture the complex dynamics in the impact regime. The nonlinearities from the electromechanical coupling, the squeeze-film damping force and the impact force are all accounted for the model. The good agreement between the simulation and experiment results indicates that the model is useful to predict the intricate behavior of the impact device and to further optimize the system in future work.

ACKNOWLEDGEMENTS

This work was supported by the Research Council of Norway through Grants no. 191282 and 229716/E20.

REFERENCES

[1] P. D. Mitcheson et al., *IEEE Proceedings*, **96** (9), pp. 1457-1486, 2008.
[2] S. Roundy, P. K. Wright, J. Rabaey, *Computer Communications*, **26**(11), pp.1131-44, 2003.
[3] M. S. M. Soliman et al., *J. Micromech. Microeng.*, **18**, 115021, 2008.
[4] D. Homann, B. Folkmer and Y. Manoli, *J. Micromech. Microeng.* **19**, 094001, 2009.
[5] H. Liu et al., *J. Microelectromech. Syst.*, **20**(5), 1131–42, 2011.
[6] M. Borowiec, G. Litak, S. Lenci, *Nonlinear Systems and Complexity*, **6**, pp. 315-321, 2014.
[7] C. P. Le, E. Halvorsen, O. Søråsen and E. M. Yeatman, *Proc. PowerMEMS* 2011, pp. 122-125, 2011.
[8] B. D. Truong, C. P. Le, E. Halvorsen, *Proc. PowerMEMS* 2014, (to be published) 2014.
[9] P. D. Mitcheson et al., *J. Microelectromech. Syst.*, **13**, pp. 429-440, 2004.
[10] C. P. Le and E. Halvorsen, *Small-Scale Energy Harvesting*, *INTECH*, pp. 265-282, 2012.
[11] M. Bao and H. Yang, *Sensors and Actuators A*, **136**, pp. 3–27, 2007.
[12] M. Machado et al., *J. Mechanism and Machine Theory,* **53**, pp. 99-121, 2012.
[13] B. N. Norden, *NBSIR* **73-243**, Institute for Basic. Standards, National Bureau of Standards, 1973.
[14] C. P. Le and E. Halvorsen, J. *Micromech. Microeng.*, **22**, 074013, 2012.

CONTACT

*Einar Halvorsen, tel: +47 33 03 77 25; Einar.Halvorsen@hbv.no